# Applying a second-kind boundary integral equation for surface tractions in Stokes flow

Eric E. Keaveny *, Michael J. Shelley

*Applied Mathematics Laboratory, Courant Institute of Mathematical Sciences, New York University, 251 Mercer Street, New York, NY 10012, USA*

**ABSTRACT**

A second-kind integral equation for the tractions on a rigid body moving in a Stokesian fluid is established using the Lorentz reciprocal theorem and an integral equation for a double-layer density. A second-order collocation method based on the trapezoidal rule is applied to the integral equation after appropriate singularity reduction. For translating prolate spheroids with various aspect ratios, the scheme is used to explore the effects of the choice of completion flow on the error in the numerical solution, as well as the condition number of the discretized integral operator. The approach is applied to obtain the velocity and viscous dissipation of rotating helices of circular cross-section. These results are compared with both local and non-local slender-body theories. Motivated by the design of artificial micro-swimmers, similar computations are performed on previously unstudied helices of non-circular cross-section to determine the dependence of the velocity and propulsive efficiency on the cross-section aspect ratio and orientation. Overall, we find that this formulation provides a stable numerical approach with which to solve the flow problem while simultaneously obtaining the surface tractions and that the appropriate choice of completion flow provides both increased accuracy and efficiency. Additionally, this approach naturally avails itself to known fast summation techniques and higher-order quadrature schemes.

© 2010 Elsevier Inc. All rights reserved.

## 1. Introduction

Boundary integral representations and the numerical methods used to solve them have been indispensable tools for the study of bodies moving in and interacting through a Newtonian Stokesian fluid. A boundary integral formulation reduces the full three-dimensional problem of solving for the fluid flow to the two-dimensional problem of determining source distributions on the bounding surfaces [1]. While numerical discretization of these equations does require the use of quadrature schemes that carefully handle singular kernels, and does produce matrices that are not sparse, complex object geometries and multiply connected domains are handled naturally [1,2], as are objects that deform or change shape in response to fluid stresses (e.g. drops, vesicles, and cells [3–10]). Additionally, techniques such as the fast multipole method [11,12] and iterative solvers such as GMRES [13] can be applied to significantly reduce the computational costs, especially for large systems.

In the case of rigid body motion, the classical boundary integral representation expresses the surface velocity as the surface convolution of the Stokeslet tensor with the surface tractions [1,14]. This first-kind integral equation for the tractions leads to poorly conditioned linear systems. Power and Miranda [15] reformulated the problem as a second-kind equation for an unknown double-layer density in a completed double-layer boundary integral equation (CDLBIE). In their formulation, the

* Corresponding author.
  *E-mail addresses:* ekeaveny@cims.nyu.edu (E.E. Keaveny), shelley@cims.nyu.edu (M.J. Shelley).

solution is represented by a surface distribution of stresslets as well as the flows generated a point force (Stokeslet) and point torque (rotlet) located within the interior of the body. The magnitude of the two point sources are related to the surface integral of the double-layer density and the surface integral of the antisymmetric moment of the double-layer density. The inclusion of Stokeslet and rotlet completes the deficient rank of the double-layer integral operator and are together referred to as the completion flow. The choice of the completion flow is not unique and other choices have been considered such as a single-layer distribution on a parallel surface in the interior of the object [16]. While use of the CDLBIE to determine the total force and torque on an object overcomes the problems of numerical stability associated with the first-kind equation, information regarding the pointwise surface tractions is not directly accessible. Knowledge of the total force and torque on the rigid body is sufficient in many applications, but there are situations, such as shape optimization [17,18], where the determination of the surface tractions is necessary. One approach to address this was pursued by Ingber and Mondy [19] who derived a second-kind integral equation involving hypersingular integrals for the tractions. Using an alternative, indirect approach, Karilla and Kim [20,2] found that it is possible to use the CDLBIE to formulate a second-kind equation for the surface tractions on a rigid body via a Lorentz reciprocal theorem argument. We refer to this equation as the completed traction boundary integral equation (CTBIE). An equation equivalent to the CTBIE was later derived [21,22] through differentiation of the single-layer first-kind equation [14] for rigid body tractions.

In this study, a second-order method based on the trapezoidal rule and the Nyström method is applied to the CTBIE. Key to this approach is the appropriate singularity reduction which is established here through a rewriting of the double-layer adjoint term. The singularity subtraction can be employed to improve the accuracy of other quadrature methods applied to the CTBIE. The scheme is employed to determine the tractions on a translating prolate spheroid, which are known exactly. These calculations are conducted for two different choices of completion flow and the differences in numerical error as well as the condition number of the resulting matrices are compared. It is found that an appropriate choice results in well conditioned systems even for bodies of high aspect ratio with GMRES needing only a very modest number of interations to determine the solution within a tolerance of $10^{-12}$. We then conduct computations to determine the translation speed of simple helical bodies of circular cross-section where we specify the angular velocity about the helical axis and require that the total force in the translation direction is zero. These results are compared with those of both local and non-local slender-body theory of [23–25]. Finally, the method is applied to determine the coefficients of the hydrodynamic mobility for helices with elliptic cross-sections. We examine the dependence of the mobility entries on the cross-sectional aspect ratio and orientation. Such a problem has not been considered previously, but is of technological importance as emerging microfluidic technologies, especially artificial micro-swimmers [26,27], are based on such shapes. Here, our results show that greater propulsion speed and mechanical efficiency can be achieved by having the major axis of the cross-section perpendicular to the helical axis.

## 2. Second-kind equation for surface tractions

For completeness, we first present the derivation of the traction integral equation for a body undergoing rigid body motion. This integral equation is established using the Lorentz reciprocal theorem and a general solution to the Stokes equations written as a completed double-layer boundary integral equation (CDLBIE).

Consider a single closed body with surface $D$ that is immersed in a three dimensional Stokesian fluid. If the surface velocity of the body is $\mathbf{v}(\mathbf{x})$, $\mathbf{x} \in D$, the fluid flow in the exterior is described by a solution to the Stokes equations

$$\nabla p - \eta \nabla^2 \mathbf{u} = \mathbf{0}, \tag{1}$$
$$\nabla \cdot \mathbf{u} = 0 \tag{2}$$

with pressure field $p$ and boundary conditions

$$\mathbf{u}(\mathbf{x}) = \mathbf{v}(\mathbf{x}), \quad \mathbf{x} \in D. \tag{3}$$

as well as $\mathbf{u}(\mathbf{x}) = \mathcal{O}(r^{-1})$ and $p(\mathbf{x}) = \mathcal{O}(r^{-2})$ as $r \to \infty$.

The Power and Miranda formulation [15], allows for $\mathbf{u}(\mathbf{x})$ to be written in terms of a double-layer density $\boldsymbol{\psi}(\mathbf{x})$ as

$$u_i(\mathbf{x}) = \int_D T_{ijk}(\mathbf{x} - \mathbf{y}) n_k(\mathbf{y}) \psi_j(\mathbf{y}) dS_{\mathbf{y}} + \mathcal{V}_i[\boldsymbol{\psi}](\mathbf{x}), \tag{4}$$

where $\mathbf{x} \in \mathbb{R}^3 \setminus \text{int}(D)$,

$$T_{ijk}(\mathbf{x} - \mathbf{y}) = \frac{3}{4\pi\eta} \frac{(x_i - y_i)(x_j - y_j)(x_k - y_k)}{|\mathbf{x} - \mathbf{y}|^5} \tag{5}$$

and $\mathbf{n}$ is the normal to the surface. Taking the limit as $\mathbf{x}$ approaches the surface in Eq. (4) yields the relationship between the known surface velocities and the double-layer density

$$v_i(\mathbf{x}) = \frac{1}{2\eta} \psi_i(\mathbf{x}) + \int_D T_{ijk}(\mathbf{x} - \mathbf{y}) n_k(\mathbf{y}) \psi_j(\mathbf{y}) dS_{\mathbf{y}} + \mathcal{V}_i[\boldsymbol{\psi}](\mathbf{x}) \tag{6}$$

with $\mathbf{x} \in D$. The term $\mathcal{V}$ in Eqs. (4) and (6) is the so-called completion flow and provides the eigenvectors necessary to have a full rank integral operator for the determination of $\boldsymbol{\psi}$. As mentioned in the introduction, there is not a unique choice for $\mathcal{V}$. While the specific choices considered in this work are presented in detail in the subsequent section, for the moment we need only to mention that the class of $\mathcal{V}$ considered in this work yields the following relationships between the double-layer density and the total force and torque on the object

$$\mathbf{F} = \int_D \boldsymbol{\psi}(\mathbf{y}) dS_{\mathbf{y}}, \tag{7}$$

$$\boldsymbol{\tau} = \int_D (\mathbf{y} - \mathbf{Y}) \times \boldsymbol{\psi} dS_{\mathbf{y}}. \tag{8}$$

with $\mathbf{Y} \in \mathrm{int}(D)$.

With Eq. (6) and the Lorentz reciprocal theorem, a second-kind equation for the tractions can be determined [2]. The Lorentz reciprocal theorem states that if two sets of flow fields and tractions on $D$, $(\mathbf{u}^1, \mathbf{f}^1)$ and $(\mathbf{u}^2, \mathbf{f}^2)$, satisfy the homogeneous Stokes equations then they also satisfy

$$\left\langle \mathbf{u}^1, \mathbf{f}^2 \right\rangle = \left\langle \mathbf{u}^2, \mathbf{f}^1 \right\rangle, \tag{9}$$

where

$$\langle \mathbf{g}, \mathbf{h} \rangle = \int_D g_i h_i dS. \tag{10}$$

Keeping solution set 1 $(\mathbf{v}, \mathbf{f})$, arbitrary and taking solution set 2 to be the flow field and tractions associated with a rigid body motion $(\mathbf{u}^{RBM}, \mathbf{f}^{RBM})$, where

$$\mathbf{u}^{RBM}(\mathbf{x}) = \mathbf{U} + \boldsymbol{\Omega} \times (\mathbf{x} - \mathbf{Y}) \tag{11}$$

for $\mathbf{x} \in D$, Eq. (9) becomes

$$\left\langle \mathbf{v}, \mathbf{f}^{RBM} \right\rangle = \left\langle \mathbf{u}^{RBM}, \mathbf{f} \right\rangle. \tag{12}$$

With the value of $\mathbf{u}^{RBM}$ on the boundary given by Eq. (11), the right hand side of Eq. (12) becomes

$$\left\langle \mathbf{u}^{RBM}, \mathbf{f} \right\rangle = \left\langle \mathbf{U} + \boldsymbol{\Omega} \times (\mathbf{x} - \mathbf{Y}), \mathbf{f} \right\rangle = \mathbf{U} \cdot \mathbf{F} + \boldsymbol{\Omega} \cdot \boldsymbol{\tau}, \tag{13}$$

where $\mathbf{F}$ and $\boldsymbol{\tau}$ are the total force and torque on the body associated with the arbitrary solution. Using Eqs. (7) and (8), this may also be written in terms of the double-layer density, $\boldsymbol{\psi}(\mathbf{x})$ corresponding to the arbitrary solution as follows:

$$\left\langle \mathbf{u}^{RBM}, \mathbf{f} \right\rangle = \mathbf{U} \cdot \mathbf{F} + \boldsymbol{\Omega} \cdot \boldsymbol{\tau} = \left\langle \mathbf{U} + \boldsymbol{\Omega} \times (\mathbf{x} - \mathbf{Y}), \boldsymbol{\psi} \right\rangle = \left\langle \mathbf{u}^{RBM}, \boldsymbol{\psi} \right\rangle. \tag{14}$$

We emphasize that $\boldsymbol{\psi}$ may be introduced in this way only because the prescribed solution is a rigid body motion, and Eqs. (7) and (8) provide the relationship between $\boldsymbol{\psi}$ and $\mathbf{F}$ and $\boldsymbol{\tau}$. The arbitrary fluid flow $\mathbf{v}(\mathbf{x})$ is also related to $\boldsymbol{\psi}(\mathbf{x})$ through Eq. (6). With the notation

$$\mathcal{A}_i[\boldsymbol{\psi}](\mathbf{x}) = \frac{1}{2\eta} \psi_i(\mathbf{x}) + \int_D K_{ij}(\mathbf{x} - \mathbf{y}) \psi_j(\mathbf{y}) dS_{\mathbf{y}} + \mathcal{V}_i[\boldsymbol{\psi}](\mathbf{x}), \tag{15}$$

the left hand side of Eq. (12) may be rewritten as

$$\left\langle \mathbf{v}, \mathbf{f}^{RBM} \right\rangle = \left\langle \mathcal{A}[\boldsymbol{\psi}](\mathbf{x}), \mathbf{f}^{RBM} \right\rangle = \left\langle \boldsymbol{\psi}, \mathcal{A}^T \left[ \mathbf{f}^{RBM} \right](\mathbf{x}) \right\rangle, \tag{16}$$

where $\mathcal{A}^T[\cdot](\mathbf{x})$ is the adjoint of the linear integral operator $\mathcal{A}[\cdot](\mathbf{x})$ and is given by

$$\mathcal{A}_i^T[\mathbf{f}](\mathbf{x}) = \frac{1}{2\eta} f_i(\mathbf{x}) + n_k(\mathbf{x}) \int_D T_{ijk}(\mathbf{y} - \mathbf{x}) f_j(\mathbf{y}) dS_{\mathbf{y}} + \mathcal{V}_i^T[\mathbf{f}](\mathbf{x}). \tag{17}$$

Combining Eqs. (14) and (16) we find

$$\left\langle \boldsymbol{\psi}, \mathcal{A}^T[\mathbf{f}^{RBM}](\mathbf{x}) - \mathbf{U} - \boldsymbol{\Omega} \times (\mathbf{x} - \mathbf{Y}) \right\rangle = 0. \tag{18}$$

Since $\boldsymbol{\psi}$ is an arbitrary double-layer density, Eq. (18) is satisfied when

$$\mathcal{A}^T \left[ \mathbf{f}^{RBM} \right](\mathbf{x}) = \mathbf{U} + \boldsymbol{\Omega} \times (\mathbf{x} - \mathbf{Y}), \tag{19}$$

yielding the second-kind completed traction boundary integral equation (CTBIE)

$$U_i + (\boldsymbol{\Omega} \times \mathbf{x})_i = \frac{1}{2\eta} f_i(\mathbf{x}) + n_k(\mathbf{x}) \int_D T_{ijk}(\mathbf{y} - \mathbf{x}) f_j(\mathbf{y}) dS_{\mathbf{y}} + \mathcal{V}_i^T[\mathbf{f}](\mathbf{x}). \tag{20}$$

Note that Eq. (20) was established for a single rigid body. This result, however, may be readily extended to interacting bodies by initially considering a CDLBIE formulated for multiply connected domains. Following the analysis described above using instead this CDLBIE in the reciprocal theorem provides the traction integral equation for the case where there are multiple bodies.

## 3. Choices of completion flow

While the double-layer integral operator combined with any appropriate choice for $\mathcal{V}$ provides a complete solution to the Stokes equations, the accuracy and conditioning of the discretized equation will depend on the specific $\mathcal{V}$. To explore these dependencies, we consider two distinct choices for $\mathcal{V}$ in our calculations of the tractions on a translating prolate spheroid presented in Section 6.1. Both choices, however, may be written in the general form

$$\mathcal{V}_i[\psi](\mathbf{x}) = \int_D G_{ij}(\mathbf{x} - \mathbf{X}(\mathbf{y}))\psi_j(\mathbf{y})dS_{\mathbf{y}} + \int_D R_{ij}(\mathbf{x} - \mathbf{X}(\mathbf{y}))((\mathbf{y} - \mathbf{X}(\mathbf{y})) \times \psi)_j dS_{\mathbf{y}}, \tag{21}$$

where the points $\mathbf{X}(\mathbf{y})$ lie in the interior of the body for all $\mathbf{y} \in D$ and

$$G_{ij}(\mathbf{x}) = \frac{1}{8\pi\eta} \left( \frac{\delta_{ij}}{|\mathbf{x}|} + \frac{x_i x_j}{|\mathbf{x}|^3} \right) \tag{22}$$

$$R_{ij}(\mathbf{x}) = \frac{1}{8\pi\eta} \frac{\epsilon_{ijk} x_k}{|\mathbf{x}|^3} \tag{23}$$

are the Stokeslet and rotlet kernels, respectively. The adjoint of the completion flow is then given by

$$\mathcal{V}_i^T[\mathbf{f}](\mathbf{x}) = \int_D G_{ji}(\mathbf{y} - \mathbf{X}(\mathbf{x}))f_j(\mathbf{y})dS_{\mathbf{y}} + \epsilon_{ijk}(x_k - X_k(\mathbf{x})) \int_D f_l(\mathbf{y})R_{lj}(\mathbf{y} - \mathbf{X}(\mathbf{x}))dS_{\mathbf{y}}. \tag{24}$$

The total force and total torque on the body for completion flow of this form are related to the double layer density through Eqs. (7) and (8), respectively.

What distinguishes the two $\mathcal{V}$ considered in this work are the details regarding $\mathbf{X}(\mathbf{y})$. For the first choice, we take $\mathbf{X}(\mathbf{y})$ to be equal to a constant position vector $\mathbf{X}_{PM}(\mathbf{y}) = \mathbf{Y}$ for some $\mathbf{Y} \in$ int $(D)$. In this case, Eq. (21) becomes

$$\mathcal{V}_{PM;i}[\psi](\mathbf{x}) = G_{ij}(\mathbf{x} - \mathbf{Y}) \int_D \psi_j(\mathbf{y})dS_{\mathbf{y}} + R_{ij}(\mathbf{x} - \mathbf{Y}) \int_D ((\mathbf{y} - \mathbf{Y}) \times \psi)_j dS_{\mathbf{y}}. \tag{25}$$

This choice of completion flow, which we call $\mathcal{V}_{PM}$, is that proposed by Power and Miranda [15] and corresponds to the flow generated by a point force and point torque located at the point $\mathbf{Y}$ in the interior of the body. The second choice we refer to as $\mathcal{V}_{SB}$ and is applicable to slender bodies whose surfaces can be parametrized by arclength $s$ and angle $\theta$ such that $\mathbf{y} = \mathbf{y}(s, \theta)$, $y \in D$. For this choice we take $\mathbf{X}_{SB}(\mathbf{y}) = \mathbf{r}(s)$ where $\mathbf{r}(s)$ is a segment of the centerline of the body. Here, the completion flow is therefore given by

$$\mathcal{V}_{SB;i}[\psi](\mathbf{x}) = \int \int G_{ij}(\mathbf{x} - \mathbf{r}(s))\psi_j(s, \theta)J(s, \theta)dsd\theta + \int \int R_{ij}(\mathbf{x} - \mathbf{r}(s))((\mathbf{y}(s, \theta) - \mathbf{r}(s)) \times \psi(s, \theta))_j J(s, \theta)dsd\theta, \tag{26}$$

where $J$ is the surface Jacobian.

## 4. Singularity subtraction

In the integrand of Eq. (20) appears the term $T_{ijk}(\mathbf{y} - \mathbf{x})n_k(\mathbf{x})$ which diverges like $1/|\mathbf{y} - \mathbf{x}|$ as $\mathbf{y} \to \mathbf{x}$ and must therefore be treated judiciously when employing numerical quadrature. Reducing the order of the singularity prior discretization is an effective approach and results in improved accuracy regardless of the choice of quadrature scheme. Such a singularity reduction is possible here using the identities

$$\int_D T_{ijk}(\mathbf{x} - \mathbf{y})n_k(\mathbf{y})dS_y = -\frac{1}{2\eta}\delta_{ij} \tag{27}$$

and

$$T_{ijk}(\mathbf{y} - \mathbf{x}) = -T_{ijk}(\mathbf{x} - \mathbf{y}), \tag{28}$$

which allow us to rewrite the first two terms in the right hand side of Eq. (20)

$$\mathcal{I}_i(\mathbf{x}) = \frac{1}{2\eta}f_i(\mathbf{x}) + n_k(\mathbf{x}) \int_D T_{ijk}(\mathbf{y} - \mathbf{x})f_j(\mathbf{y})dS_{\mathbf{y}} \tag{29}$$

as

$$\mathcal{I}_i(\mathbf{x}) = \int_D T_{ijk}(\mathbf{y} - \mathbf{x})(f_j(\mathbf{y})n_k(\mathbf{x}) + f_j(\mathbf{x})n_k(\mathbf{y}))dS_{\mathbf{y}}. \tag{30}$$

As shown in Appendix A, this reformulation of the adjoint double-layer removes the $1/|\mathbf{y} - \mathbf{x}|$ divergence of the kernel. While this reduction technique is similar to that for the double-layer integral [1,15] and relies on the same identity Eq. (27), the resulting form of the integrand is quite different. The most striking difference is the plus sign in the integrand in Eq. (30) as opposed to the minus sign in the regularized double-layer integral [1].

## 5. Numerical discretization

While the integrand in Eq. (30) does not diverge as $\mathbf{y} \to \mathbf{x}$, its value will depend on the direction from which the limit is taken. This type of "phase" singularity is similar to that encountered in the Biot-Savart integral in 2D vortex dynamics and an effective technique to handle this integral numerically is the point vortex method [28,29]. In the point vortex method, the integral is approximated using the trapezoidal rule where the contribution from the source whose location coincides with the field point is removed from the trapezoidal sum. This modification has been shown to preserve the second-order accuracy [28,29] of the trapezoidal rule, and is widely used in discretizations of the CDLBIE. We employ the approach here for the CTBIE with our numerical results presented in Section 6.1 indicating second-order accuracy.

Before applying the trapezoidal rule to $\mathcal{I}$ and $\mathcal{V}^T$, a surface parametrization $(u, v)$ is introduced so that Eq. (30) becomes

$$\mathcal{I}_i(\mathbf{y}(u, v)) = \int \int T_{ijk}(\mathbf{y}(u', v') - \mathbf{y}(u, v))(f_j(u', v')n_k(u, v) + f_j(u, v)n_k(u', v'))J(u', v')du'dv', \tag{31}$$

while Eq. (24) now reads

$$\mathcal{V}_i^T[\mathbf{f}](\mathbf{y}(u, v)) = \int \int G_{ji}(\mathbf{y}(u', v') - \mathbf{X}(u, v))f_j(u', v')J(u', v')du'dv' + \epsilon_{ijk}(y_k(u, v)$$
$$- X_k(u, v)) \int \int f_l(u, v)R_{lj}(\mathbf{y}(u', v') - \mathbf{X}(u, v))J(u', v')du'dv'. \tag{32}$$

where $\mathbf{x} = \mathbf{y}(u, v)$ and $J$ is the surface Jacobian. We then introduce the rectangular surface mesh $u_p = ph_1$ and $v_q = qh_2$ where $h_1$ is the grid spacing in the $u$ – direction, $h_2$ is the grid spacing in the $v$ – direction and $p = 1, \ldots, N_u$ while $q = 1, \ldots, N_v$. Taking the field point to coincide with the grid point $(u_n, v_m)$, we then apply the trapezoidal rule to Eqs. (31) and (32) to obtain,

$$\mathcal{I}_i^h(u_n, v_m) = h_1 h_2 \sum_{p \neq n}{}' \sum_{q \neq m}{}' \left[ T_{ijk}(\mathbf{y}(u_p, v_q) - \mathbf{y}(u_m, v_n)) \times (f_j(u_p, v_q)n_k(u_n, v_m) + f_j(u_n, v_m)n_k(u_p, v_q))J(u_p, v_q) \right] \tag{33}$$

and

$$\mathcal{V}_i^{T,h}[\mathbf{f}](u_n, v_m) = h_1 h_2 \sum_p{}' \sum_q{}' \left[ G_{ji}(\mathbf{y}(u_p, v_q) - \mathbf{X}(u_n, v_m))f_j(u_p, v_q) + \epsilon_{ijk}(y_k(u_n, v_m) \right.$$
$$\left. - X_k(u_n, v_m))f_l(u_p, v_q)R_{lj}(\mathbf{y}(u_p, v_q) - \mathbf{X}(u_n, v_m)) \right]J(u_p, v_q), \tag{34}$$

where $\sum'$ indicates the trapezoidal sum where the endpoints are weighted by a factor of 1/2. Eq. (20) evaluated at the field point $\mathbf{y}(u_n, v_m)$ is then replaced by

$$U_i + \epsilon_{ijk}\Omega_j y_k(u_n, v_m) = \mathcal{I}_i^h(u_n, v_m) + \mathcal{V}_i^{T,h}(u_n, v_m). \tag{35}$$

For prescribed motion of the boundary, Eq. (35) may be expressed as the linear system of equations

$$\mathcal{U} = \mathcal{A}^{T,h}\mathcal{F}, \tag{36}$$

where $\mathcal{U}$ is the vector containing the three components of the velocity at each of the $N_{pts}$ collocation points, $\mathcal{F}$ is the unknown traction data at the collocation points, and the $3N_{pts} \times 3N_{pts}$ matrix $\mathcal{A}^{T,h}$ is the discretized integral operator.

## 6. Numerical simulations

In this section, the numerical scheme described above is used to determine the tractions on a prolate spheroid translating parallel and perpendicular to its axis of symmetry and to calculate the motion of helices with both circular and ellipsoidal cross-sections. In the case of the prolate spheroid, exact expressions for the tractions and the total force are known [30,31], allowing for the study of the convergence of the numerical solution for different choices of completion flow. For helices with circular cross-section, we can compare our numerical results with those determined from local [24,25] and non-local [23] slender-body theories.

### 6.1. Settling prolate spheroid

As a first test of the numerical scheme, the tractions on prolate spheroids of different aspect ratios translating with velocity **U** in directions parallel and perpendicular to its axis of symmetry are calculated and compared with analytic expressions obtained from Oberbeck's solution [30,31]. The surface of a spheroid whose axis of symmetry is aligned with the $z$-direction may be expressed as

$$\mathbf{x}(\phi, \theta) = a \sin \phi \cos \theta \hat{\mathbf{x}} + a \sin \phi \sin \theta \hat{\mathbf{y}} - c \cos \phi \hat{\mathbf{z}}, \tag{37}$$

where $\phi \in [0, \pi]$ and $\theta \in [0, 2\pi]$. For translation velocity $\mathbf{U} = U\hat{\mathbf{z}}$ parallel to the axis of symmetry, the surface tractions are of the form $\mathbf{f}_\parallel = f_\parallel(\phi)\hat{\mathbf{z}}$ where

$$f_\parallel(\phi) = \frac{4U\eta}{\chi_0 + \alpha_0 c^2} \left[ \frac{\cos^2 \phi}{c^2} \epsilon^2 + \frac{1}{a^2} \right]^{-1/2} \tag{38}$$

and $\epsilon = \sqrt{c^2 - a^2}/c^2$. For translation $\mathbf{U} = U\hat{\mathbf{x}}$ perpendicular to the axis of symmetry, the surface tractions are given by $\mathbf{f}_\perp = f_\perp(\phi)\hat{\mathbf{x}}$ with

$$f_\perp(\phi) = \frac{4U\eta}{\chi_0 + \alpha_1 a^2} \left[ \frac{\cos^2 \phi}{c^2} \epsilon^2 + \frac{1}{a^2} \right]^{-1/2}. \tag{39}$$

The constants in Eqs. (38) and (39) are

$$\chi_0 = \frac{ca^2}{\sqrt{c^2 - a^2}} \mathcal{L}, \tag{40}$$

$$\alpha_0 = \frac{ca^2}{(c^2 - a^2)^{3/2}} \mathcal{L} - \frac{2a^2}{c^2 - a^2}, \tag{41}$$

$$\alpha_1 = \frac{c^2}{c^2 - a^2} - \frac{ca^2}{2(c^2 - a^2)^{3/2}} \mathcal{L}. \tag{42}$$

where $\mathcal{L} = \log[(1 + \epsilon)/(1 - \epsilon)]$. The tractions given by Eqs. (38) and (39) for $c/a \in [2, 32]$ are plotted as the solid lines in Fig. 1. For motion both parallel and perpendicular to the axis, the variation in magnitude of the tractions between the poles and equator increases with increasing aspect ratio. The total force on the prolate spheroid,

$$\mathbf{F} = \int \mathbf{f}(\mathbf{y}) dS_\mathbf{y} \tag{43}$$

for parallel motion is then given by

$$\mathbf{F} = F_\parallel \hat{\mathbf{z}} = \frac{16\pi c \epsilon^3 U}{(1 + \epsilon^2)\mathcal{L} - 2\epsilon} \hat{\mathbf{z}} \tag{44}$$

and for the perpendicular case by

$$\mathbf{F} = F_\perp \hat{\mathbf{x}} = \frac{32\pi c \epsilon^3 U}{(3\epsilon^2 - 1)\mathcal{L} + 2\epsilon} \hat{\mathbf{x}}. \tag{45}$$

With the surface described by Eq. (37), $u = \phi$ and $v = \theta$ are taken in Eqs. (31) and (32). The tractions are then determined numerically from the discretized system Eq. (35) with $N_\phi + 1$ points in the $\phi$-direction and $N_\theta$ points in the $\theta$-direction. Accounting for the redundancy of the poles, the total number of points is $N_{pts} = (N_\phi - 1)N_\theta + 2$. To explore the dependence of the numerical solution on the specific choice of completion flow, the two choices for $\mathcal{V}$ from Section 3 are considered in our calculations. For $\mathcal{V}_{PM}$, we take $\mathbf{X}_{PM} = (0, 0, 0)$. As the centerline of the spheroid is described by the $z$-coordinate, for the slender-body choice, $\mathcal{V}_{SB}$ we take $\mathbf{X}_{SB}(\phi) = -\epsilon c \cos \phi \hat{\mathbf{z}}$ for the surface point **x**. Scaling by the eccentricity $\epsilon$ ensures $\mathbf{X}_{SB}(\phi)$ lies in the interior of the spheroid $\forall \phi \in [0, \pi]$.

For all the calculations presented here, the linear system Eq. (36) is solved directly and $N_\theta = 4$ while $N_\phi$ is varied from $N_\phi = 4 - 512$ yielding grid sizes $h_1 = \pi/N_\phi$ and $h_2 = 2\pi/N_\theta$. Over this range of $N_\phi$, a negligible decrease in the error was observed when $N_\theta$ was increased to $N_\theta = 8$. This suggests a weak dependence of the error on $N_\theta$.

The values of the tractions determined numerically for $N_\phi = 256$ and with $\mathcal{V}_{SB}$ are shown as circular markers in Fig. 1 and are in excellent agreement with the analytic solutions Eqs. (38) and (39). To analyze the convergence of the numerical solution, $\tilde{f}$, the $L_2$-error in the tractions

$$E_2(h_1) = \|f - \tilde{f}\|_{2,N_\phi} = \left( h_1 \sum_n' |f - \tilde{f}|^2 \right)^{1/2} \tag{46}$$

is computed.
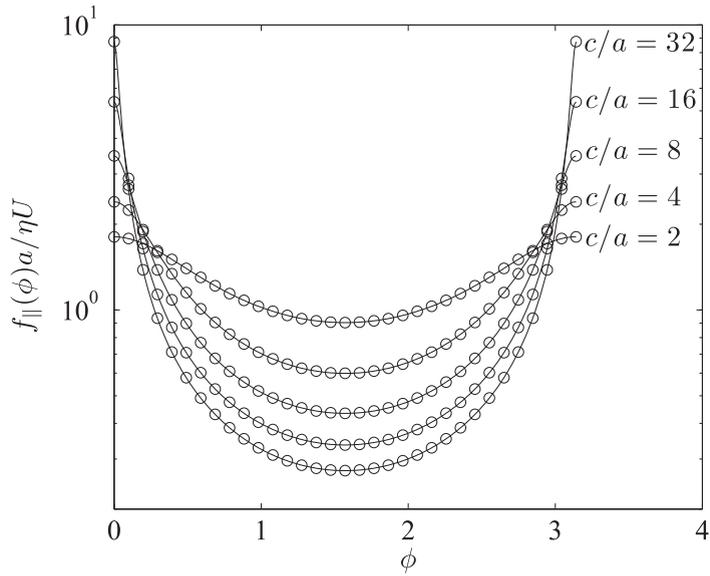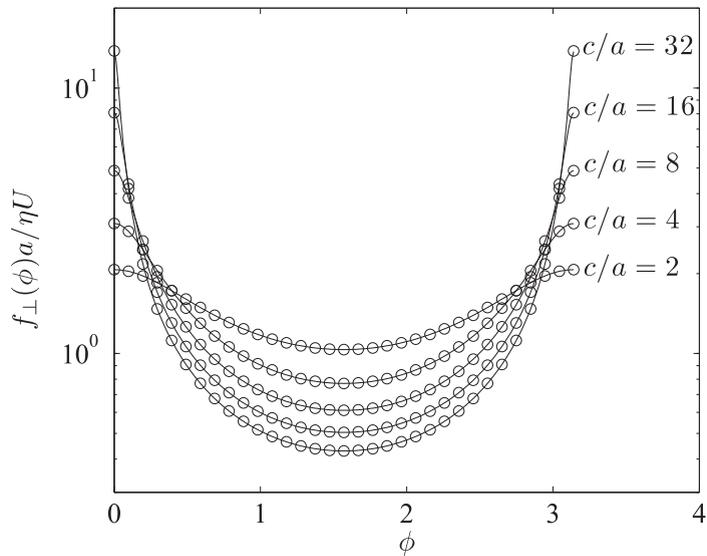
**Fig. 1.** The tractions on a prolate spheroid translating (a) parallel and (b) perpendicular to its axis of symmetry. The solid lines are provided by the analytic solution and the circular symbols correspond to simulation results where $N_\phi = 256$ and $\mathcal{V}_{SB}$. The aspect ratio of the spheroid, $c/a$, for each case is indicated.

The values of the relative $L_2$-error, $E_2/\|f\|_{2,N_\phi}$, for both parallel and perpendicular motions for $\mathcal{V}_{PM}$ and $\mathcal{V}_{SB}$ are shown in Fig. 2. For both choices of completion flow and for both parallel and perpendicular motions, second-order accuracy is observed and confirmed by calculating

$$p(h_1) = \frac{1}{\log 2} \log \left[ E_2(2h_1)/E_2(h_1) \right]. \tag{47}$$

For a given discretization, however, the choice of $\mathcal{V}_{PM}$ is found to provide a more accurate solution especially for the higher aspect ratio cases. For the choice $\mathcal{V}_{PM}$, we also observe rapid decrease in the error before the asymptotic convergence rate is achieved. For finer discretizations, the error in the numerical solution using $\mathcal{V}_{PM}$ appears to depend less on the aspect ratio than it does for $\mathcal{V}_{SB}$. The error in the total force
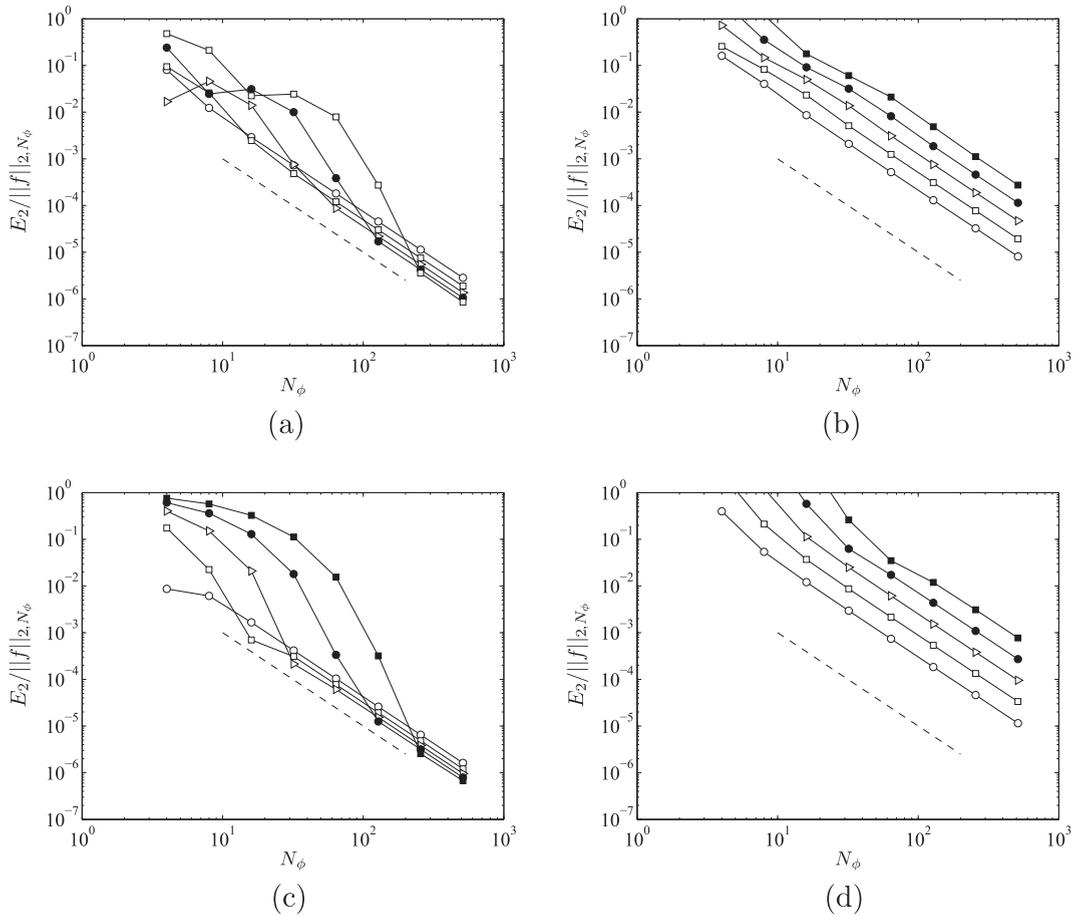
**Fig. 2.** $E_2/\|f\|_{2,N_\phi}$ as a function of $N_\phi$ for (a) and (b) parallel and (c) and (d) perpendicular translations. (a) and (c) were provided with $\mathcal{V}_{PM}$ and (b) and (d) correspond to the choice $\mathcal{V}_{SB}$. In the plots: open circles indicate $c/a$ = 2, open squares $c/a$ = 4 and open triangles $c/a$ = 8 while closed circles correspond to $c/a$ = 16 and closed squares to $c/a$ = 32. The dashed lines in each figure indicate second-order convergence.

$$\Delta F_{\|,\perp} = \left| F_{\|,\perp} - h_1 h_2 \sum_n{}' \sum_m{}' \tilde{f}_{\|,\perp}(\phi_n, \theta_m) J(\phi_n, \theta_m) \right| \tag{48}$$

is also determined for the two choices of completion flow. These data are shown in Fig. 3, and here the calculations with the slender body completion flow, $\mathcal{V}_{SB}$, provide the more accurate value of the total force. We again observe second-order accuracy and a more rapid convergence before the asymptotic rate is realized. For the case where the spheroid is settling parallel to its axis, we see small dips in the curves before asymptotic convergence is reached. This is due to the difference between the analytical and numerical force values changing sign from positive to negative and ultimately converging to zero from below. In looking at the normalized pointwise error in Fig. 4, one finds a constant value for $\mathcal{V}_{PM}$ and a variation over approximately five orders of magnitude for $\mathcal{V}_{SB}$ with the maximum error realized near the poles. The error is much greater than that of the $\mathcal{V}_{PM}$ case near the poles, but is less near the equator. The large increase in the error near the poles for $\mathcal{V}_{SB}$ is a result of an evaluation point for the completion flow being close to the surface of the spheroid. This hypothesis was confirmed by taking $\mathcal{V}_{PM}$ with $\mathbf{X}_{PM} = (0,0,c\epsilon)$ and observing similar values in the error. In the calculation of the force, the Jacobian appears in the integral and it decreases to zero near the poles. Therefore, the main contribution to the error in the force, $\Delta F$, comes from the equatorial values where the $\mathcal{V}_{SB}$ choice provides a better estimate.

In Figs. 2 and 3, a rapid convergence to second-order accuracy is observed, especially for low values of the aspect ratio. We expect that the order of the next term in the error expansion is of higher order than $h^3$. Assuming the error expansion may be written as

$$E_2(h_1) = C_2 h_1^2 + C_q h_1^q + \mathcal{O}(h_1^r), \tag{49}$$

where $r > q > 2$, we also have

$$E_2(2h_1) = 4C_2 h_1^2 + 2^q C_q h_1^q + \mathcal{O}(h_1^r). \tag{50}$$
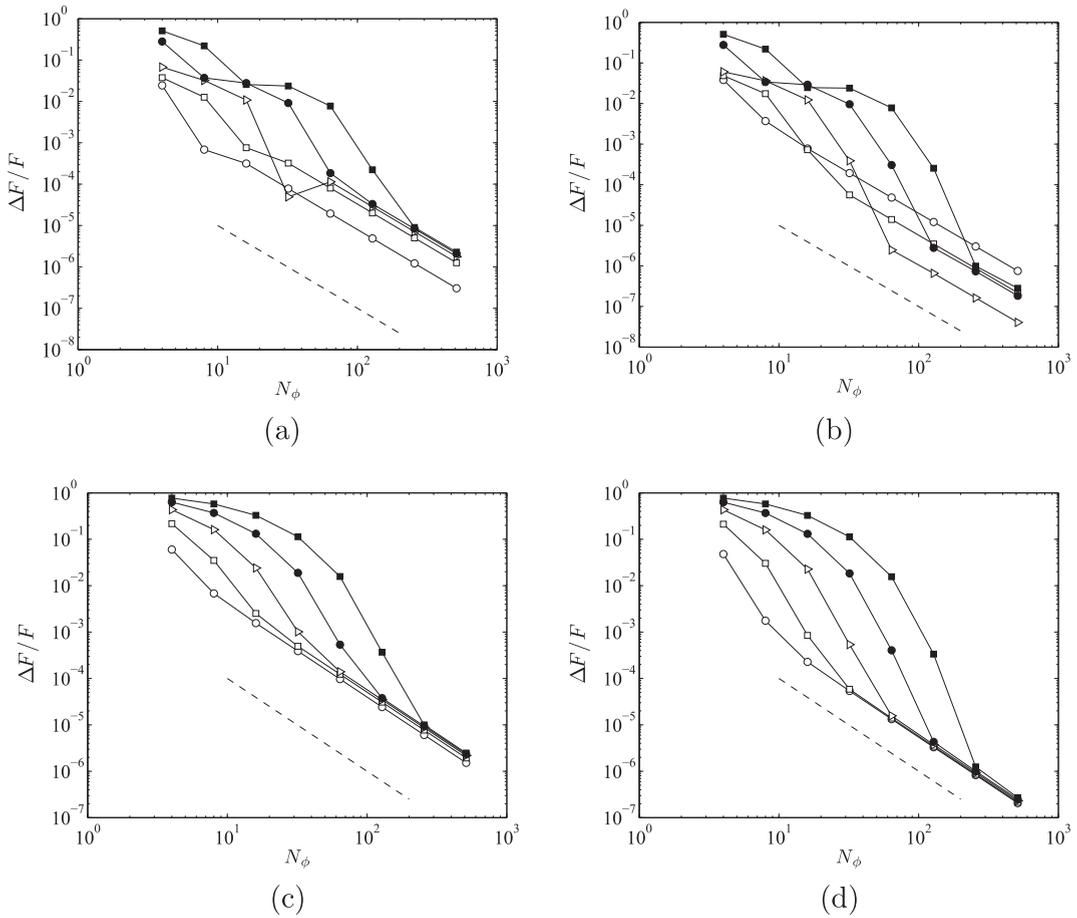
**Fig. 3.** $\Delta F/F$ as a function of $N_\phi$ for (a) and (b) parallel and (c) and (d) perpendicular translations. (a) and (c) were provided with $\mathcal{V}_{PM}$ and (b) and (d) correspond to the choice $\mathcal{V}_{SB}$. In the plots: open circles indicate $c/a = 2$, open squares $c/a = 4$ and open triangles $c/a = 8$ while closed circles correspond to $c/a = 16$ and closed squares to $c/a = 32$. The dashed lines in each figure indicate second-order convergence.
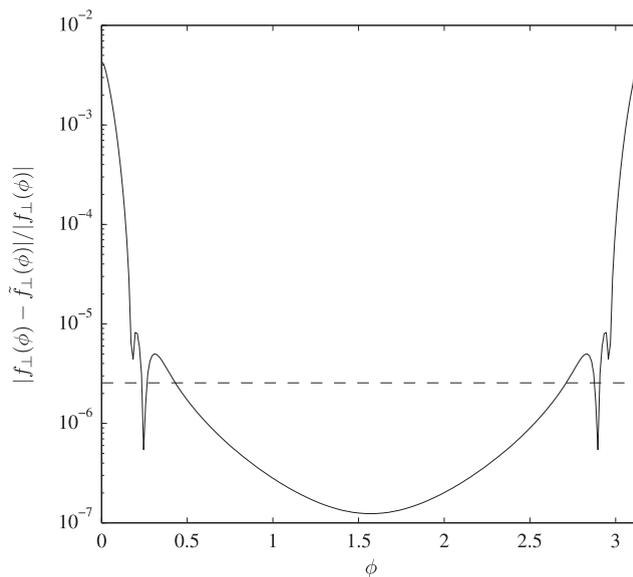


**Fig. 4.** Pointwise error in the tractions as a function of $\phi$ for $c/a = 32$ and $N_\phi = 256$. The solid line corresponds to $\mathcal{V}_{SB}(\mathbf{x})$ and the dashed line to $\mathcal{V}_{PM}(\mathbf{x})$.

**Table 1**
Exponent of the next order correction, $q$, for $\mathcal{V}_{SB}$ for the case of translation parallel to the axis of symmetry, as $N_\phi$ and aspect ratio $c/a$ are varied.

| $N_\phi$ | $c/a$ | | |
|---|---|---|---|
| | 2 | 4 | 8 |
| 128 | 4.0353 | 4.1941 | 4.3235 |
| 256 | 4.0086 | 4.0388 | 4.1977 |
| 512 | 4.0021 | 4.0094 | 4.0390 |

**Table 2**
Exponent of the next order correction, $q$, for $\mathcal{V}_{SB}$ for the case of translation perpendicular to the axis of symmetry, as $N_\phi$ and aspect ratio $c/a$ are varied.

| $N_\phi$ | $c/a$ | | |
|---|---|---|---|
| | 2 | 4 | 8 |
| 128 | 4.0113 | 4.0404 | 3.3854 |
| 256 | 4.0017 | 4.0050 | 3.9889 |
| 512 | 4.00016 | 3.999958 | 3.9943 |

**Table 3**
Condition number when the completion flow is $\mathcal{V}_{PM}$, as $N_\phi$ and aspect ratio $c/a$ are varied.

| $N_\phi$ | $c/a$ | | | | |
|---|---|---|---|---|---|
| | 2 | 4 | 8 | 16 | 32 |
| 8 | 2.0765e1 | 3.6687e2 | 1.9657e4 | 1.9223e6 | 2.3391e8 |
| 16 | 2.1662e1 | 3.9955e2 | 1.5352e4 | 9.4858e5 | 9.5275e7 |
| 32 | 2.2216e1 | 4.2412e2 | 1.6429e4 | 7.5191e5 | 4.9691e7 |
| 64 | 2.2519e1 | 4.3647e2 | 1.7262e4 | 7.9205e5 | 3.9386e7 |
| 128 | 2.2679e1 | 4.4275e2 | 1.7666e4 | 8.2663e5 | 4.1089e7 |
| 256 | 2.2760e1 | 4.4592e2 | 1.7868e4 | 8.4320e5 | 4.2730e7 |

Using Eqs. (49) and (50), we may determine the order of the correction term in the error expansion from

$$q(h_1) = \frac{1}{\log 2} \log \left[ (E_2(4h_1) - 4E_2(2h_1)) / (E_2(2h_1) - 4E_2(h_1)) \right]. \tag{51}$$

Values of $q$ are shown in Tables 1 and 2 for $\mathcal{V}_{SB}(\mathbf{x})$, $c/a = 2 - 8$ and $N_\phi = 128 - 512$ and indicate that the next term in the error expansion is fourth-order. Although not reported, the same result was found for $\mathcal{V}_{PM}$. This does suggest that higher-order schemes could easily be found through Richardson extrapolation or through direct calculation and removal of the second-order error term [29].

Like the values of the error, the condition numbers of the matrices resulting from the discretization of the integral operators will depend on the choice of completion flow. The condition number for the case of $\mathcal{V}_{PM}$ are given in Table 3, while those corresponding to $\mathcal{V}_{SB}$ are given in Table 4. For both choices of completion flow, we find the method to be well-conditioned in that the condition number is not found to greatly increase with mesh refinement. We do find, however, that for larger aspect ratios, the condition number when $\mathcal{V} = \mathcal{V}_{SB}$ is significantly less than that when we take $\mathcal{V} = \mathcal{V}_{PM}$. For the most extreme case of $c/a = 32$ and $N_\phi = 256$, the condition number for the $\mathcal{V}_{PM}$ case is about $5 \times 10^5$ times greater than the value 80.363 for $\mathcal{V}_{SB}$. While the condition number of the matrix illustrates how sensitive the solution of a linear system is to perturbations in the right hand side data, it may not be directly associated with the number of iterations needed by a Kyrlov subspace method to determine the solution to the system within a given tolerance [32,33]. We therefore directly explore the number of GMRES [13] iterations required for convergence. Tables 5 and 6 show the number of GMRES iterations needed to determine the tractions on a prolate spheroid translating perpendicular to its axis for when the completion flow choices are $\mathcal{V}_{PM}$ and $\mathcal{V}_{SB}$, respectively. In these calculations, the relative tolerance was $10^{-12}$ and the aspect ratio varied from $c/a = 2$ to $c/a = 32$. Additionally, these GMRES computations were performed without restarting or preconditioning. As was the case when examing the condition number, we see that for both choices of completion flow, the number of interations does not grow significantly as the mesh is refined, but the number of interations does increase with increasing aspect ratio. The growth with aspect ratio is much slower for the case where $\mathcal{V}_{SB}$. In the most extreme case where $c/a = 32$, it requires nearly four times fewer iterations for when we have $\mathcal{V}_{SB}$ than for $\mathcal{V}_{PM}$.

Fig. 5 shows the spectrum of $\mathcal{A}^{T,h}$ for the two choices of completion flow for the case where $N_\phi = 256$ and $c/a = 32$. While the values of the spectral radii for the two choices are comparable, we find that the modulus of the minimum eigenvalue of $\mathcal{A}^{T,h}$ with $\mathcal{V}_{PM}$ is several orders of magnitude less than that when we take $\mathcal{V}_{SB}$. As the aspect ratio of the body increases, so

**Table 4**
Condition number when the completion flow is $\mathcal{V}_{SB}$, as $N_\phi$ and aspect ratio $c/a$ are varied.

| $N_\phi$ | $c/a$ | | | | |
|---|---|---|---|---|---|
| | 2 | 4 | 8 | 16 | 32 |
| 8 | 4.3208e0 | 8.2001e0 | 3.8178e1 | 4.8251e2 | 1.2495e4 |
| 16 | 4.5461e0 | 7.4470e0 | 1.6442e1 | 5.6977e1 | 5.5242e2 |
| 32 | 4.5744e0 | 7.4716e0 | 1.6581e1 | 3.4579e1 | 8.8530e1 |
| 64 | 4.5829e0 | 7.5318e0 | 1.6867e1 | 3.6452e1 | 7.2310e1 |
| 128 | 4.5864e0 | 7.5778e0 | 1.7087e1 | 3.7415e1 | 7.7866e1 |
| 256 | 4.7171e0 | 7.6053e0 | 1.7224e1 | 3.8013e1 | 8.0363e1 |

**Table 5**
Number of GMRES iterations needed (without preconditioning or restarting) to determine the tractions to within a tolerance of $10^{-12}$ on a prolate spheroid of aspect ratio $c/a$ translating perpendicular to its axis of symmetry when the completion flow is $\mathcal{V}_{PM}$.

| $N_\phi$ | $c/a$ | | | | |
|---|---|---|---|---|---|
| | 2 | 4 | 8 | 16 | 32 |
| 8 | 12 | 14 | 17 | 26 | 36 |
| 16 | 17 | 21 | 28 | 40 | 73 |
| 32 | 21 | 23 | 33 | 55 | 99 |
| 64 | 22 | 25 | 34 | 60 | 108 |
| 128 | 23 | 27 | 37 | 61 | 120 |
| 256 | 24 | 28 | 40 | 63 | 117 |
| 512 | 24 | 29 | 40 | 66 | 120 |

**Table 6**
Number of GMRES iterations needed (without preconditioning or restarting) to determine the tractions to within a tolerance of $10^{-12}$ on a prolate spheroid of aspect ratio $c/a$ translating perpendicular to its axis of symmetry when the completion flow is $\mathcal{V}_{SB}$.

| $N_\phi$ | $c/a$ | | | | |
|---|---|---|---|---|---|
| | 2 | 4 | 8 | 16 | 32 |
| 8 | 12 | 12 | 12 | 11 | 12 |
| 16 | 16 | 17 | 20 | 23 | 22 |
| 32 | 19 | 17 | 22 | 26 | 32 |
| 64 | 21 | 19 | 22 | 27 | 34 |
| 128 | 21 | 20 | 22 | 27 | 34 |
| 256 | 22 | 20 | 23 | 27 | 34 |
| 512 | 24 | 20 | 23 | 27 | 35 |
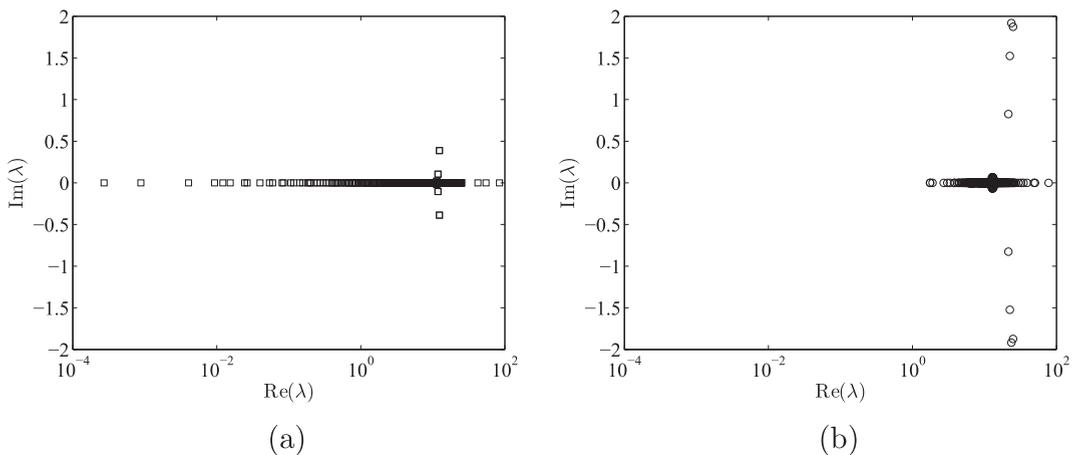


**Fig. 5.** Spectrum of $\mathcal{A}^{T,h}$ for (a) $\mathcal{V}_{PM}$ and (b) $\mathcal{V}_{SB}$ where in each case $N_\phi = 256$ and $c/a = 32$.

does the ratio of the largest to smallest eigenvalues of the adjoint double-layer operator. The growth of this ratio may be regulated by choosing $\mathcal{V}_{SB}$ whose spectrum intersects that of the double-layer. The spectrum of $\mathcal{V}_{PM}$ does not intersect that of the double-layer operator and therefore does not have this property.

## 6.2. Helix with a circular cross-section

A more complex shape to be considered here is a rigid simple helix with a circular cross-section. Given their importance in low Reynolds number swimming and the locomotion of microorganisms such as *E. coli* [34–36], simple helices have been studied experimentally [35,37,38], computationally [39] and theoretically [24,25,23] with the latter two using a variety of resistive force and slender-body theories.

A helical curve parametrized by its arclength $s \in [-l, l]$ and whose axis is aligned with the *z*-direction may be written as

$$\mathbf{R}(s) = \beta(\cos ks \hat{\mathbf{x}} + \sin ks \hat{\mathbf{y}}) + \alpha s \hat{\mathbf{z}} \tag{52}$$

with $|d\mathbf{R}/ds|^2 = \alpha^2 + \beta^2 k^2$. The parameter $\beta$ describes the radius of the helix, while $k$ and $\alpha$ provide the wavelength $\Lambda = 2\pi/k$ and helical pitch $\lambda = \alpha\Lambda$. These parameters are related through the condition $|d\mathbf{R}/ds|^2 = 1$ so the unit tangent vector to the curve is given by $\hat{\mathbf{t}} = d\mathbf{R}/ds$.

In [24], a continuous distribution of Stokeslets along $\mathbf{R}$ is considered and the resulting integrals are evaluated in the limit where the centerline curvature is zero and the force density is constant over a lengthscale $q$. The lengthscale $q$ is assumed to be small relative to the total length of the helix, $L = 2l$, but large relative to the radius of the cross-section, $a$. The resulting formula are used to explore the motion of the helix in the zero-thrust limit where the motion of the centerline is given by

$$\mathbf{V}(s) = (-\Omega\beta\sin ks, \ \Omega\beta\cos ks, \ U) \tag{53}$$

and the total force in the *z*-direction is zero, $\mathbf{F} \cdot \hat{\mathbf{z}} = 0$. For a prescribed angular velocity $\Omega$, the resulting velocity $U$ and the torque per unit length $\mathbf{T} = T\hat{\mathbf{z}}$ and viscous dissipation per unit length $E/L = T\Omega$ are determined over a range of $\beta^2 k^2$ for the values of the slenderness parameter $\Lambda/a$ = 50, 100 and 200.

To compare with the results from [24,25], we consider a helix with four turns, $k = 4\pi$ and a prolate spheroidal longitudinal cross-section. The surface of such a helix may be described as

$$\mathbf{x}(\phi, \theta) = \mathbf{R}(s(\phi)) + r(s(\phi))(\cos\theta\hat{\mathbf{N}} + \sin\theta\hat{\mathbf{B}}) \tag{54}$$

with

$$\hat{\mathbf{N}} = \cos\gamma\hat{\mathbf{n}} + \sin\gamma\hat{\mathbf{b}}, \tag{55}$$
$$\hat{\mathbf{B}} = -\sin\gamma\hat{\mathbf{n}} + \cos\gamma\hat{\mathbf{b}}, \tag{56}$$
$$\gamma(s) = -\alpha ks, \tag{57}$$
$$s = -l\cos\phi. \tag{58}$$

where $\hat{\mathbf{n}} = (1/\kappa)(d\mathbf{t}(s)/ds)$ is the normal to the curve in the Frenet–Serret frame, $\hat{\mathbf{b}} = \hat{\mathbf{t}} \times \hat{\mathbf{n}}$ is the binormal unit vector, $\kappa = |d\mathbf{t}/ds|$ is the curvature of the centerline, and $r(s) = a\sqrt{1 - s^2/l^2}$ is radius of the cross section. This parametrization leads to an orthogonal coordinate system as $\partial\mathbf{x}/\partial\phi \cdot \partial\mathbf{x}/\partial\theta = 0$ and the use of the variable $\phi$ rather than $s$ clusters collocation points near the poles where higher resolution is needed. The CTBIE is solved to determine the tractions and the unknown velocity $U$ for the mixed boundary conditions $\mathbf{U} = (0, 0, U)$, $\boldsymbol{\Omega} = (0, 0, 1)$ and $\mathbf{F} \cdot \hat{\mathbf{z}} = 0$ using $\mathcal{V}_{SB}$ with $\mathbf{X}_{SB} = \epsilon\mathbf{R}$ where $\epsilon = \sqrt{(l^2 - a^2)/l}$. For each case $\Lambda/a$ = 50, 100 and 200, $N_\theta = 4$ however for $\Lambda/a$ = 50, $N_\phi = 512$ is considered, for $\Lambda/a$ = 100 we have $N_\phi = 1024$ and finally for $\Lambda/a$ = 200, $N_\phi = 2048$. After discretizing, we solve the linear system using preconditioned GMRES [13]. We found that an effective preconditioner $\mathcal{P}$ consists of the $2N_d + 1$ diagonals of the matrix $\mathcal{A}^{T,h}$ in Eq. (36). Specifically, we take

$$\mathcal{P}_{ij} = \begin{cases} \mathcal{A}_{ij}^{T,h}, & |i - j| \leqslant N_d, \\ 0, & |i - j| > N_d. \end{cases} \tag{59}$$

Here, we use a value of $N_d = 300$ for which GMRES needed only 13 interations to converge to within a tolerance of $10^{-8}$ for the case where $\Lambda/a$ = 100 and $N_\phi = 1024$.

Fig. 6 shows the values of the speed normalized by the wave speed, $Uk/\alpha\Omega$, the dimensionless torque per unit length, $T/4\pi\eta\beta^2\Omega$ and the normalized viscous dissipation per unit length $E/\eta L U^2$ taken from [24,25] and calculated using the discretized CTBIE. Despite the various assumptions [24,25] introduced in the formulation of the local slender-body theory, the determined values of $Uk/\alpha\Omega$, $T/4\pi\eta\beta^2\Omega$ and $E/\eta LU^2$ agree quite well with those calculated here for helices of finite length with variable longitudinal cross section. The simulations and local slender body theory predict the same trends in the data including maximum efficiency occurring at $\beta^2 k^2 \approx 0.45$. The main discrepancy occurs in the value of $T/4\pi\eta\beta^2\Omega$ at lower values of $\beta^2 k^2$ for $\Lambda/a$ = 50. For this case, the helix is nearly straight and the torque about the finite cross-section of the body plays a role in determining the overall value of the force moment. The importance of these torques decreases as $\Lambda/a$ increases, and one again sees correspondence between the two calculations.

The simulation results may also be compared with those of non-local slender-body theory [23]. This theory is based on the asymptotic expansion of the integral

$$\mathbf{u}(\mathbf{x}) = \int_{-\epsilon l}^{\epsilon l} G_{ij}(\mathbf{x} - \mathbf{X}(s))\bar{f}_j(s) + \nabla^2 G_{ij}(\mathbf{x} - \mathbf{X}(s))\bar{g}_j(s)ds \tag{60}$$
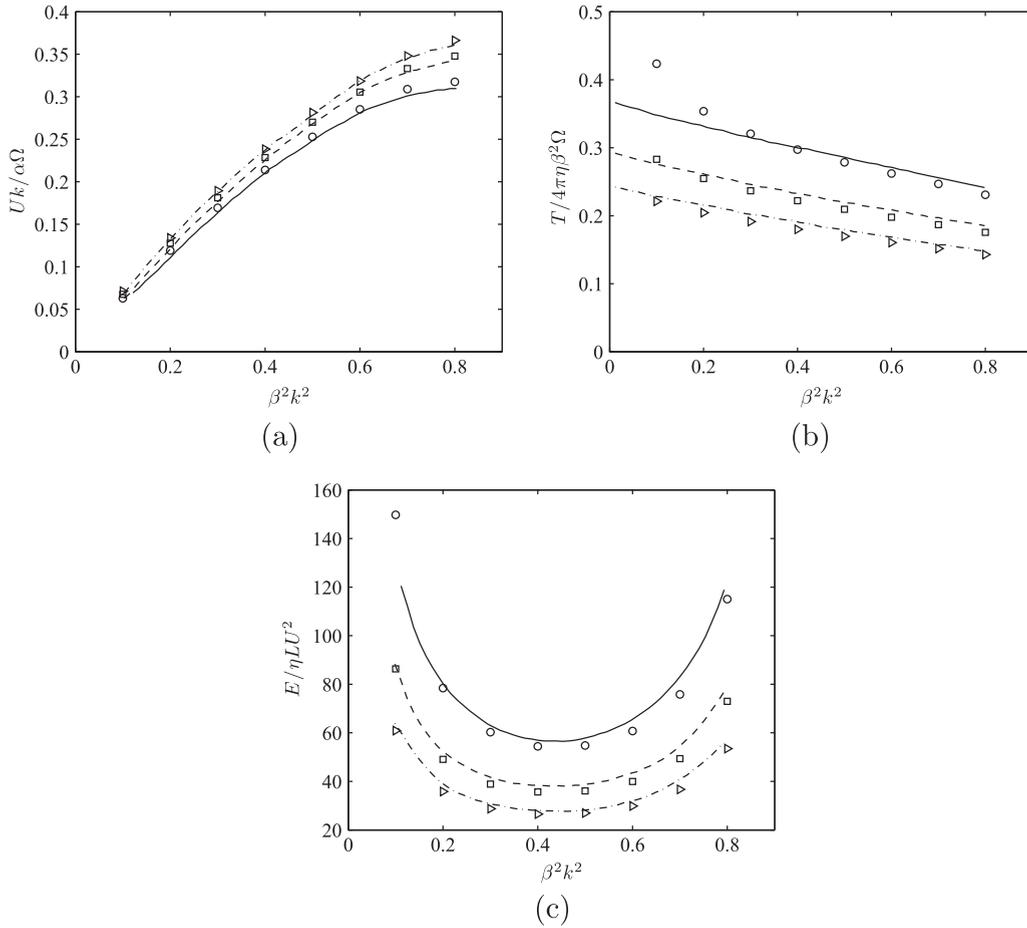
**Fig. 6.** A comparison of the (a) nomalized velocity, (b) normalized torque per unit length, and (c) normalized viscous dissipation per unit length between local slender-body theory [25] (lines) and the numerical simulation (symbols). In the plots, the solid line and circular markers correspond to the case where $\Lambda/a = 50$, the dashed line and square symbols to $\Lambda/a = 100$, and the dash-dotted line and triangular markers indicate the case where $\Lambda/a = 200$.

in the limit where $a/l \ll 1$. Here, the flow is represented by a distribution of Stokeslets and source doublets along the centerline of the body. This theory allows for the calculation of the force per unit length $\bar{\mathbf{f}}(s)$ on a slender body of finite length and specified longitudinal cross-section. Johnson [23] provides calculations of zero-thrust values of $\bar{\mathbf{f}}(s)$ for helices of prolate spheroidal longitudinal cross-section with $\beta/\lambda = 0.01$ and $a/\lambda = 0.25$ for $k = \pi$ and $k = 5\pi$ corresponding to one and five turns respectively. Computations are performed of these same cases using the surface parametrization, completion flow and GMRES tolerance and preconditioner as before with $N_\theta = 4$ and $N_\phi = 512$ for $k = \pi$ and $N_\phi = 2048$ for $k = 5\pi$. The force per unit length is determined from

$$\bar{\mathbf{f}}(s) = \int_0^{2\pi} \mathbf{f}(s,\theta) J(s,\theta) d\theta. \tag{61}$$

Shown in Fig. 7 are the values of $\bar{f}_t = \hat{\mathbf{t}} \cdot \bar{\mathbf{f}}, \bar{f}_n = \hat{\mathbf{n}} \cdot \bar{\mathbf{f}}$ and $\bar{f}_b = \hat{\mathbf{b}} \cdot \bar{\mathbf{f}}$ as a function of $s$ provided by Johnson [23] as well as those determined here. Additionally depicted are the values of $\bar{\mathbf{f}}(s)$ determined using the resistive force theory for helices introduced in [24]

$$C_t = \frac{2\pi\eta}{\log(2q/r(s))}, \tag{62}$$

$$C_b = \frac{4\pi\eta}{\log(2q/r(s)) + 1/2}, \tag{63}$$

such that $\bar{f}_t = C_t(\mathbf{V} \cdot \hat{\mathbf{t}})$ and $\bar{f}_b = C_b(\mathbf{V} \cdot \hat{\mathbf{b}})$ with $q = 0.09\Lambda$. The effect of the longitudinal variation in the cross-section are introduce by having $r(s)$ rather than $a$ in the expressions for the drag coefficients. Excellent correspondence is found between the values determined in [23] and the simulations. Additionally, one begins to see convergence to the values predicted by the resistive force theory as the number of turn is increased from one to five.
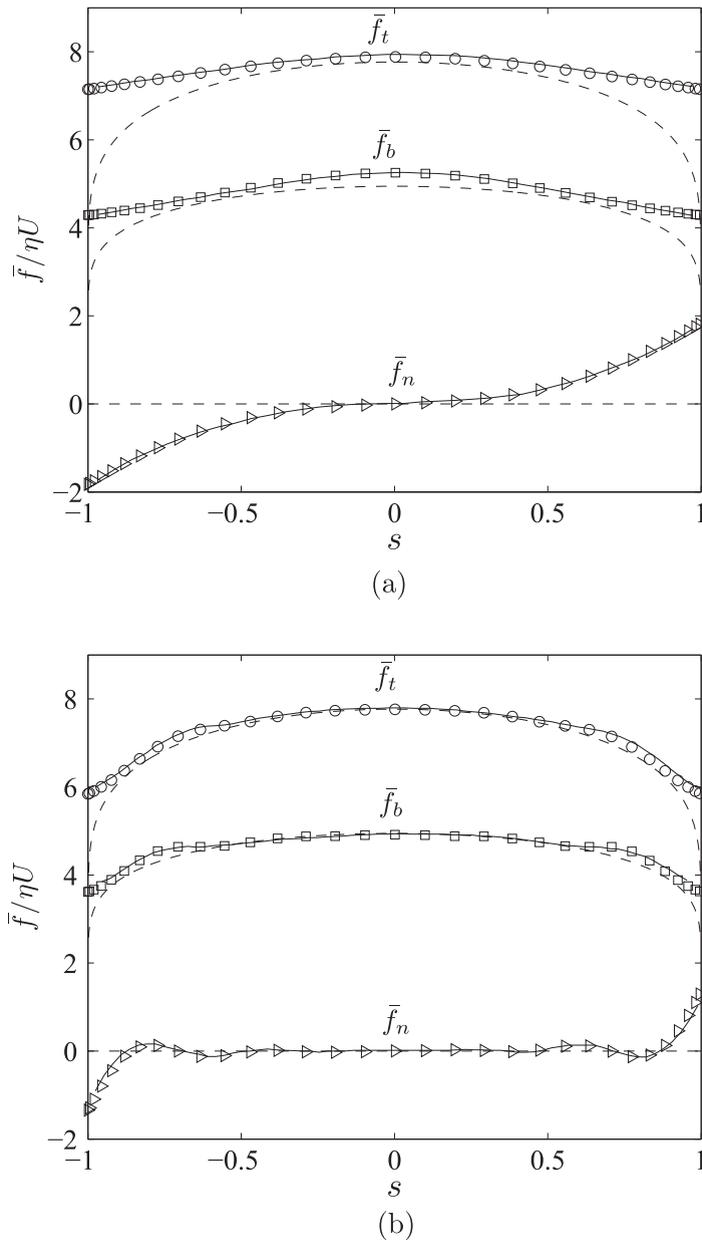
**Fig. 7.** A comparison of the force per unit length on helices with prolate spheroidal longitudinal cross section between those given by slender-body theory of [23] (solid line), resistive force theory (dashed line) and the numerical simulations (markers). In (a) $k = \pi$, $\beta/\lambda = 0.25$ and $a/\lambda = 0.1$ and for (b) $k = 5\pi$, $\beta/\lambda = 0.25$ and $a/\lambda = 0.1$.

### 6.3. Helices with non-circular cross-section

While helices with circular cross-sections have been studied extensively, less is known about other shapes that couple rotation and translation at low Reynolds number. Such shapes are important in emerging microfluidic technologies, especially the development of artificial micro-swimmers such as those constructed in [26,27]. Presented in this section are computations for shapes similar to those of the micro-swimmers in [26,27] whose centerlines are simple helices, but whose cross-sections are an ellipses. The surfaces of the objects considered are given by

$$\mathbf{x}(\phi, \theta) = \mathbf{R}(s(\phi)) + r_N(s(\phi)) \cos \theta \widehat{\mathbf{N}} + r_B(s(\phi)) \sin \theta \widehat{\mathbf{B}} \tag{64}$$

with

$$\widehat{\mathbf{N}} = \cos \gamma \hat{\mathbf{n}} + \sin \gamma \hat{\mathbf{b}}, \tag{65}$$
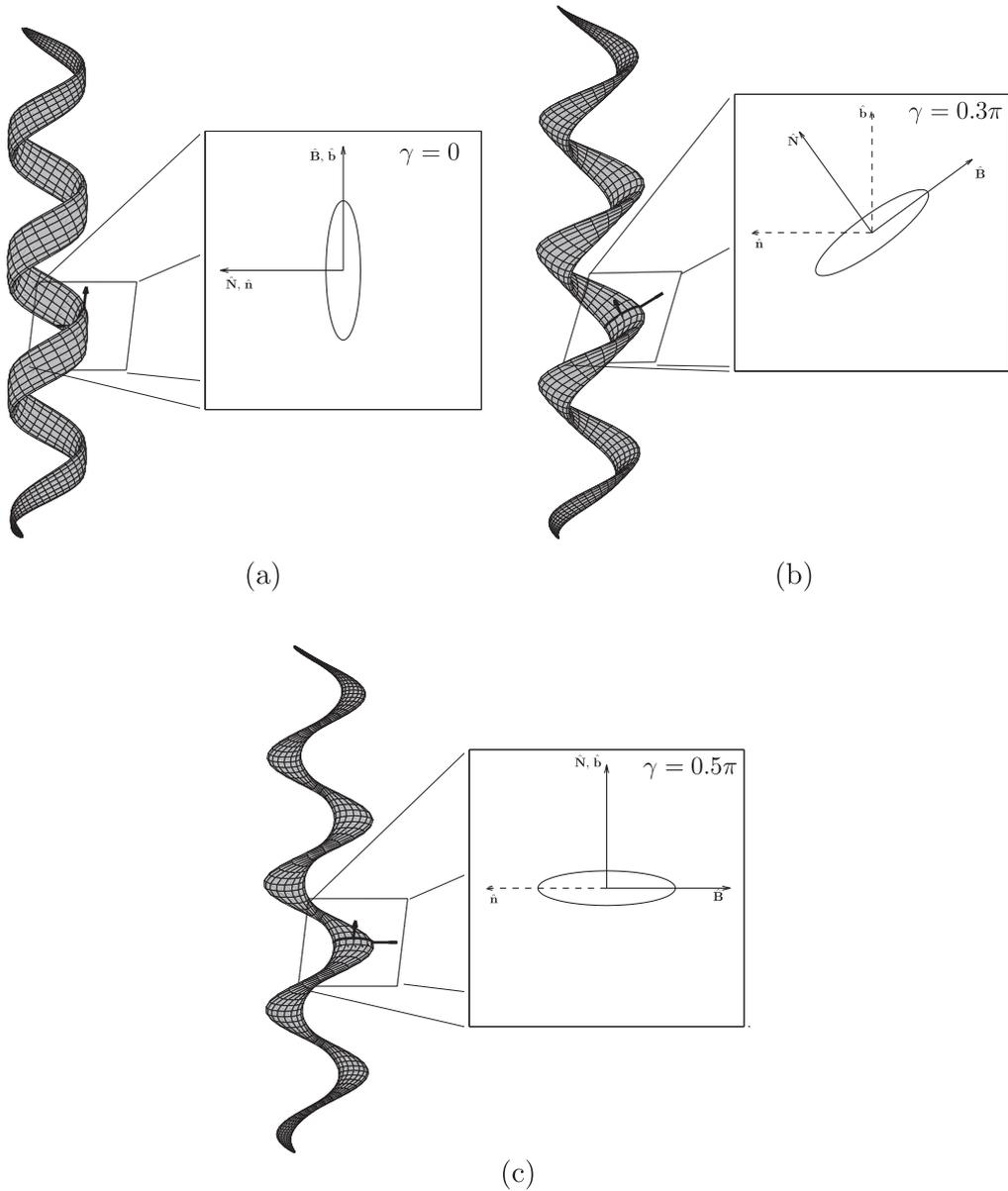
**Fig. 8.** Images of helices with non-circular cross-sections for which $\alpha = 0.5$, $k = 4\pi$, and $a_B/a_N = 4$. Each image corresponds to a different value of the cross-section orientation parameter: (a) $\gamma = 0$, (b) $\gamma = 0.3\pi$, and (c) $\gamma = 0.5\pi$. The inset associated with each image shows the orientation of the cross-section relative to the normal, $\hat{\mathbf{n}}$, and binormal, $\hat{\mathbf{b}}$, vectors.

$$\widehat{\mathbf{B}} = -\sin\gamma\hat{\mathbf{n}} + \cos\gamma\hat{\mathbf{b}}, \tag{66}$$

$$r_N(s) = a_N\sqrt{1 - s^2/l^2}, \tag{67}$$

$$r_B(s) = a_B\sqrt{1 - s^2/l^2}. \tag{68}$$

Here, the parameter $\gamma$ controls the orientation of the cross-section. Images of helices described Eqs. (65)–(68) with $a_N/a_B = 4$, $\alpha = 0.5$ and $k = 4\pi$ for three different values of $\gamma$ are depicted in Fig. 8. Additionally, the longitudinal aspect ratio is $a/l = 50$ where $a^2 = a_N a_B$.

Mobility calculations are performed where $\mathbf{F} = \mathbf{0}$ and $\boldsymbol{\tau} = \hat{\mathbf{z}}$ to explore the dependence of the velocity-torque entry of the mobility matrix, $M_B$ where $U = M_B\tau$ with $U = \mathbf{U} \cdot \hat{\mathbf{z}}$. We also examine a measure of mechanical efficiency, $\eta l\, U^2/E$ with viscous dissipation $E = \boldsymbol{\tau}\cdot\boldsymbol{\Omega}$, on the cross-section aspect ratio and orientation. Higher values of $M_B$ correspond to helices that yield
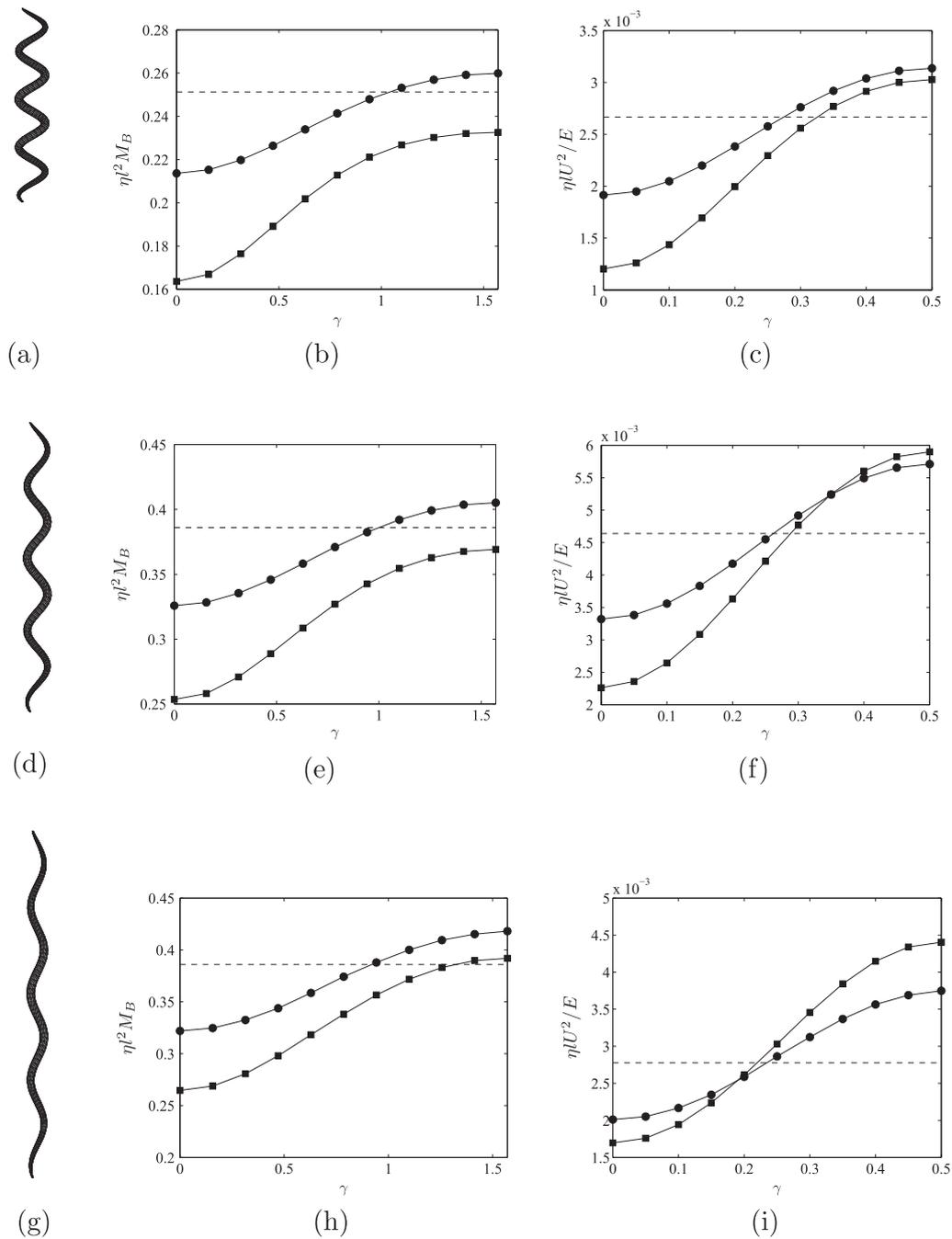
**Fig. 9.** The figures show images of helices with a circular cross-section of radius $a$ as well as the values of $M_B$ and the efficiency $\eta l U^2/E$ as a function of $\gamma$. In (a)–(c) $\alpha = 0.5$, (d)–(f) $\alpha = 0.75$, and (g)–(i) $\alpha = 0.9$. In the plots, the solid line with the closed circular markers indicates values for $a_N/a_B = 2$, the solid line with the closed square markers corresponds to $a_B/a_N = 4$ and the dashed line indicates the values for a circular cross-section.

higher swimming speeds for a given torque, while higher values of $\eta l\, U^2/E$ correspond to more efficient propellers. These calculations are performed for helices with three different values of $\alpha = 0.5$, 0.75, and 0.9 and $k = 4\pi$, see Fig. 9(a), (d) and (g). For each, we consider cross-sectional aspect ratios $a_B/a_N = 1$, 2 and 4 with $a_B a_N = a^2$ fixed and values of orientation parameter $\gamma$ over the range $\gamma \in [0, 0.5\pi]$. The simulations are performed using $\mathcal{V}_{SB}$ with $\mathbf{X}_{SB} = \epsilon \mathbf{R}$, $N_\theta = 16$, $N_\phi = 256$. Once again, we employ preconditioned GMRES to solve the linear system with the same preconditioner $\mathcal{P}$ with $N_d = 300$ as described in Eq. (59) in the previous section. Here, 19 iterations were needed for the solution to converge within a tolerance of $10^{-8}$ for the case where $\alpha = 0.75$ and $\gamma = 0$.

Fig. 9 shows the values of $M_B$ and $\eta l U^2/E$ determined from the simulations. In general, the values of $M_B$ and the efficiency are lower for the helices of ellipsoidal cross-section with smaller values of $\gamma$ than those helices with circular cross-sections. These helices, see Fig. 8(a), closely resemble the shape achieved by wrapping a ribbon around a pencil. In the worst case where $a_B/a_N = 4$, $\gamma = 0$ and $\alpha = 0.5$, one sees a 35% reduction in the value of $M_B$ and an efficiency of less than half that of the circular case. A non-circular cross-section with a higher value of $\gamma$, however, can improve both the performance and efficiency of a helical drive. These helices (see Fig. 8(c)) are similar to the auger-like shapes used in Archimedes' screws. We find the greatest enhancement in efficiency ($\approx 60\%$) for the case where $\alpha = 0.9$, $\gamma = \pi/2$ and $a_N/a_B = 4$, where as the largest increase in speed per unit torque of about 10% occurs for $\alpha = 0.9$, $\gamma = \pi/2$ and $a_N/a_B = 2$.

## 7. Conclusions

In this study, calculations of the tractions on rigid bodies in Stokes flow are performed using a second-kind integral equation for the tractions. This CTBIE was derived using a second-kind equation for a double-layer density and the Lorentz reciprocal theorem, see also [20,2]. The appropriate singularity reduction for the adjoint double-layer integral operator was presented and applied to the CTBIE. With the singularity reduced, the CTBIE was discretized using the trapezoidal rule resulting in a second-order collocation scheme. The tractions on translating prolate spheroids of various aspect ratios are computed and compared with the analytic solutions. These calculations were performed for two choices of the completion flow. The first choice, $\mathcal{V}_{PM}$, corresponds to that considered in [15], while the second choice $\mathcal{V}_{SB}$ is provided by a distribution of Stokeslets and rotlets along the centerline of the object. For both choices of completion flow, second-order accuracy was observed as was a fourth-order correction term in the error expansion. While $\mathcal{V}_{PM}$ gave better accuracy for the traction data, $\mathcal{V}_{SB}$ provided better accuracy for the total force on the spheroid and yielded well conditioned matrices even for spheroids with high aspect ratios. In examining the motion of simple helices with circular cross-sections in the zero-thrust limit, general agreement was found with the local slender body theoretic results of [24,25] while excellent agreement was observed with force per unit length calculations based on non-local slender-body theory [23]. We then explored the dependence of the velocity-torque coupling and propulsion efficiency of helices with non-circular cross-section on the aspect ratio and orientation of the cross-section. These results have direct implications in the design and construction of artificial micro-swimmers such as those presented in [26,27]. Our calculations indicate that when the major axis of the cross-section is perpendicular to the helical axis, greater speed and efficiency can be achieved compared to helices with a circular cross-section. On the other hand, reduced speed and higher energy costs are observed when the major axis is nearly aligned with the helical axis. There is, therefore, a clear advantage for micro-swimmers that resemble Archimedes' screws over those that are similar in shape to a strip of paper wrapped around a circular rod.

While the numerical scheme presented here has been shown to be an effective means to calculate the tractions on a rigid body, several improvements can be made to improve the accuracy of the solution. Higher-order discretizations such as those based on spectral elements [40] or those employing floating partitions of unity [41] are applicable here, especially for the regularized integral provided in this work. Another route to obtaining higher-order accuracy would entail determining explicitly the leading order term in error expansion for the trapezoidal rule approximation and subtracting off its contribution [29]. The numerical results here suggest the subtracting off the leading order term would result in fourth-order accurate scheme. In addition to improving the accuracy of the numerical solution, the computational work may also be reduced. Pairwise, $\mathcal{O}(N_{pts}^2)$ calculations were used here to determine the discrete integral operator. Methods such as the fast-multipole method [11] or particle-mesh Ewald [42] can be implemented to decrease the computational work especially when the number of quadrature points exceeds $10^4$ [12]. Here, we examined how both accuracy of the numerical solution as well as the condition number of the linear system depend on the choice of completion flow in comparing two specific cases. Conducting numerical experiments with the CTBIE for other choices of completion flow that have been introduced [16] that allow for more general considerations in the shape of the surface is of interest and is perhaps an initial step toward establishing a general protocol for how to appropriately choose the completion flow. While the CTBIE can be applied to objects of a variety of shapes, the boundary conditions are limited to rigid body motion. Extending the Lorentz reciprocal theorem argument for non-rigid body boundary conditions [2] and obtaining numerical solutions for these equations are also subjects for future studies. This method is currently being applied by us to the problem of shape optimization for micro-swimmers (in preparation).

## Acknowledgments

## Appendix A. Singularity reduction

To show that the integrand in the adjoint double-layer in Eq. (20) is bounded as $\mathbf{y} \to \mathbf{x}$, surface coordinates $u$ and $v$ with $\mathbf{x} = \mathbf{y}(u_0, v_0)$ are adopted so that

$$\mathcal{I} = \int \int T_{ijk}(\mathbf{y}(u,v) - \mathbf{y}_0)(f_j(u,v)n_{0,k} + f_{0,j}n_k(u,v))J(u,v)dudv \tag{A.1}$$

with $\mathbf{y}_0 = \mathbf{y}(u_0, v_0)$, $\mathbf{n}_0 = \mathbf{n}(u_0, v_0)$, and $\mathbf{f}_0 = \mathbf{f}(u_0, v_0)$. Expanding the integrand about the point $(u_0, v_0)$ one obtains

$$\mathbf{y}(u,v) - \mathbf{y}_0 = \Delta u \frac{\partial \mathbf{y}}{\partial u}\bigg|_0 + \Delta v \frac{\partial \mathbf{y}}{\partial v}\bigg|_0 + \frac{1}{2}\left((\Delta u)^2 \frac{\partial^2 \mathbf{y}}{\partial u^2}\bigg|_0 + 2\Delta u \Delta v \frac{\partial^2 \mathbf{y}}{\partial u \partial v}\bigg|_0 + (\Delta v)^2 \frac{\partial^2 \mathbf{y}}{\partial v^2}\bigg|_0\right) + \mathcal{O}(\rho^3), \tag{A.2}$$

$$\mathbf{n}(u,v) = \mathbf{n}_0 + \Delta u \frac{\partial \mathbf{n}}{\partial u}\bigg|_0 + \Delta v \frac{\partial \mathbf{n}}{\partial v}\bigg|_0 + \mathcal{O}(\rho^2), \tag{A.3}$$

$$\mathbf{f}(u,v) = \mathbf{f}_0 + \Delta u \frac{\partial \mathbf{f}}{\partial u}\bigg|_0 + \Delta v \frac{\partial \mathbf{f}}{\partial v}\bigg|_0 + \mathcal{O}(\rho^2) \tag{A.4}$$

with $\rho = \sqrt{\Delta u^2 + \Delta v^2}$, $\Delta u = u - u_0$ and $\Delta v = v - v_0$. Since the surface normal may be expressed as

$$n_i(u,v) = \frac{1}{J(u,v)}\epsilon_{ijk}\frac{\partial y_j}{\partial u}\frac{\partial y_k}{\partial v} \tag{A.5}$$

its partial derivatives are

$$\frac{\partial n_i}{\partial u} = \frac{1}{J}(\delta_{il} - n_i n_l)\epsilon_{ljk}\left(\frac{\partial^2 y_j}{\partial u^2}\frac{\partial y_k}{\partial v} + \frac{\partial y_j}{\partial u}\frac{\partial^2 y_k}{\partial u \partial v}\right), \tag{A.6}$$

$$\frac{\partial n_i}{\partial v} = \frac{1}{J}(\delta_{il} - n_i n_l)\epsilon_{ljk}\left(\frac{\partial^2 y_j}{\partial v \partial v}\frac{\partial y_k}{\partial v} + \frac{\partial y_j}{\partial u}\frac{\partial^2 y_k}{\partial v^2}\right) \tag{A.7}$$

and the following identities hold

$$\mathbf{n} \cdot \frac{\partial \mathbf{y}}{\partial u} = 0, \tag{A.8}$$

$$\mathbf{n} \cdot \frac{\partial \mathbf{y}}{\partial v} = 0, \tag{A.9}$$

$$\frac{\partial \mathbf{n}}{\partial u} \cdot \frac{\partial \mathbf{y}}{\partial u} = -\mathbf{n} \cdot \frac{\partial^2 \mathbf{y}}{\partial u^2}, \tag{A.10}$$

$$\frac{\partial \mathbf{n}}{\partial v} \cdot \frac{\partial \mathbf{y}}{\partial v} = -\mathbf{n} \cdot \frac{\partial^2 \mathbf{y}}{\partial v^2}, \tag{A.11}$$

$$\frac{\partial \mathbf{n}}{\partial v} \cdot \frac{\partial \mathbf{y}}{\partial u} = -\mathbf{n} \cdot \frac{\partial^2 \mathbf{y}}{\partial u \partial v}, \tag{A.12}$$

$$\frac{\partial \mathbf{n}}{\partial u} \cdot \frac{\partial \mathbf{y}}{\partial v} = -\mathbf{n} \cdot \frac{\partial^2 \mathbf{y}}{\partial u \partial v}. \tag{A.13}$$

After substituting Eqs. (A.2)–(A.4) into Eq. (A.1) and combining terms using the identities Eqs. (A.10)–(A.13), one finds that the leading order term in an expansion of the integrand of the about the field point $\mathbf{x} = \mathbf{y}(u_0, v_0)$ can expressed as

$$P_i(\Delta u_1, \Delta u_2) = \frac{\zeta_i^{\alpha\beta\gamma\delta\epsilon}\Delta u_\alpha \Delta u_\beta \Delta u_\gamma \Delta u_\delta \Delta u_\epsilon}{\left|\Delta u_\xi \frac{\partial \mathbf{y}}{\partial u_\xi}(u_0, v_0)\right|^5}, \tag{A.14}$$

where $\Delta u_1 = \Delta u$ and $\Delta u_2 = \Delta v$. In Eq. (A.14), the Greek indices have values 1 and 2 and their repetition implies summation. The matrix coefficient, $\zeta_i^{\alpha\beta\gamma\delta\epsilon}$, depends on the values of $\mathbf{y}$, $\mathbf{n}$, $\mathbf{f}$, surface Jacobian $J$ and derivatives of these functions at $(u_0, v_0)$. We see that both the numerator and denominator of the integrand decay to zero like $\mathcal{O}(\rho^5)$ as $\mathbf{y} \to \mathbf{x}$ and therefore attains a finite value in the limit $\mathbf{y} \to \mathbf{x}$. While finite, the tensorial dependence in the numerator indicates that the value will depend on the direction from which the limit is taken.

## References

[1] C. Pozrikidis, Boundary Integral and Singularity Methods for Linearized Viscous Flow, Cambridge University Press, 1992.
[2] S. Kim, S.J. Karrila, Microhydrodynamics: Principles and Selected Applications, Dover Publications, Inc., 2005.
[3] C. Pozrikidis, Numerical studies of cusp formation at fluid interfaces in Stokes flow, J. Fluid Mech. 357 (1998) 29–57.
[4] M. Kropinski, An efficient numerical method for studying interfacial motion in two-dimensional creeping flows, J. Comput. Phys. 171 (2001) 479–508.
[5] M. Kropinski, Numerical methods for multiple inviscid interfaces in creeping flows, J. Comput. Phys. 180 (2002) 1–24.
[6] S. Veerapeneni, D. Geuyffier, D. Zorin, G. Biros, A boundary integral method for simulating the dynamics of inextensible vesicles suspended in a viscous fluid in 2D, J. Comput. Phys. 228 (2009) 2334–2353.
[7] S. Veerapeneni, D. Geuyffier, G. Biros, D. Zorin, A numerical method for simulating the dynamics of 3D axisymmetric vesicles suspended in viscous flows, J. Comput. Phys. 228 (2009) 7233–7249.
[8] J.S. Sohn, Y.-H. Tseng, S. Li, A. Voigt, J.S. Lowengrub, Dynamics of multicomponent vesicles in a viscous fluid, J. Comput. Phys. 229 (2010) 119–144.
[9] C. Pozrikidis, The axisymmetric deformation of a red blood cell in a uniaxial straining Stokes flow, J. Fluid Mech. 216 (1990) 231–254.

[10] H. Zhao, A. Isfahani, L. Olson, J. Freund, A spectral boundary integral method for flowing blood cells, J. Comput. Phys. 229 (2010) 3726–3744.
[11] L. Greengard, V. Rokhlin, A fast algorithm for particle simulations, J. Comput. Phys. 73 (1987) 325–348.
[12] A.-K. Tornberg, L. Greengard, A fast multipole method for the three-dimensional Stokes equations, J. Comput. Phys. 227 (2008) 1613–1619.
[13] Y. Saad, M. Schultz, GMRES: a generalized minimal residual algorithm for solving nonsymmetric linear systems, SIAM J. Sci. Stat. Comput. 7 (3) (1986) 856–869.
[14] G. Youngren, A. Acrivos, Stokes flow past a particle of arbitrary shape: a numerical method of solution, J. Fluid Mech. 69 (1975) 377–403.
[15] H. Power, G. Miranda, Second kind integral equation formulation of Stokes' flows past a particle of arbitrary shape, SIAM J. Appl. Math. 47 (4) (1987) 689–698.
[16] O. Gonzalez, On stable, complete, and singularity-free boundary integral formulations of exterior Stokes flow, SIAM J. Appl. Math. 69 (4) (2009) 933–958.
[17] O. Pironneau, Optimal Shape Design for Elliptic Systems, Springer-Verlag, 1984.
[18] S.W. Walker, M.J. Shelley, Shape optimization of peristaltic pumping, J. Comput. Phys. 229 (4) (2010) 1260–1291.
[19] M. Ingber, L. Mondy, Direct second kind boundary integral formulation for Stokes flow problems, Comput. Mech. 11 (1993) 11–27.
[20] S. Karilla, S. Kim, Integral equations of the second kind for Stokes flow: direct solution for physical variables and removal of inherent accuracy limitations, Chem. Eng. Commun. 82 (1989) 123–161.
[21] N. Liron, E. Barta, Motion of a rigid particle in Stoke flow: a new second-kind boundary-integral equation formulation, J. Fluid Mech. 238 (1992) 579–598.
[22] S. Kim, H. Power, A note on two boundary integral formulations for particle mobilities in Stokes flow, J. Fluid Mech. 257 (1993) 637–639.
[23] R. Johnson, An improved slender-body theory for Stokes flow, J. Fluid Mech. 99 (1980) 411–431.
[24] J. Lighthill, Flagellar hydrodynamics: the John von Neumann lecture, 1975, SIAM Rev. 18 (2) (1976) 161–230.
[25] J. Lighthill, Helical distributions of Stokeslets, J. Eng. Math. 30 (1996) 35–78.
[26] A. Ghosh, P. Fischer, Controlled propulsion of artificial magnetic nanostructured propellers, Nano Lett. 9 (6) (2009) 2243–2245.
[27] L. Zhang, J. Abbott, L. Dong, B. Kratochvil, D. Bell, B. Nelson, Artificial bacterial flagella: fabrication and magnetic control, Appl. Phys. Lett. 94 (2009) 064107.
[28] J. Goodman, T. Hou, J. Lowengrub, Convergence of the point vortex method for the 2D Euler equations, Commun. Pur. Appl. Math. 43 (1990) 415–430.
[29] J. Lowengrub, M. Shelley, B. Merriman, High-order and efficient methods for the vorticity formulation of the Euler equations, SIAM J. Sci. Comput. 14 (5) (1993) 1107–1142.
[30] A. Oberbeck, Ueber stationäre flüssigkeitsbewegungen mit berücksichtigung der inneren reibung, J. Reine Angew. Math. 81 (1876) 62–80.
[31] H. Lamb, Hydrodynamics, Dover Publications, Inc., 1945.
[32] N.M. Nachtigal, S.C. Reddy, L.N. Trefethen, How fast are nonsymmetric matrix iterations, SIAM J. Matrix Anal. Appl. 13 (1992) 778–795.
[33] M. Embree, How descriptive are GMRES convergence bounds? Tech. rep., Oxford University Computing Laboratory, 1999.
[34] H. Berg, Bacteria swim by rotating their flagellar filaments, Nature 245 (1973) 380.
[35] E. Purcell, Life at low Reynolds number, Am. J. Phys. 45 (1) (1977) 3–11.
[36] H. Flores, E. Lobaton, S. Méndez-Diez, S. Tlupova, R. Cortez, A study of bacterial flagellar bundling, Bull. Math. Biol. 67 (2005) 137–168.
[37] E. Purcell, The efficiency of propulsion by a rotating flagellum, Proc. Natl. Acad. Sci. USA 87 (1997) 4895.
[38] S. Jung, K. Mareck, L. Fauci, M. Shelley, Rotational dynamics of a superhelix towed in a Stokes fluid, Phys. Fluids 19 (2007) 103105.
[39] R. Cortez, L. Fauci, A. Medovikov, The method of regularized Stokeslets in three dimensions: analysis, validation and application to helical swimming, Phys. Fluids 17 (2005) 031504.
[40] G. Muldowney, J. Higdon, A spectral boundary element approach to three-dimensionaly Stokes flow, J. Fluid Mech. 298 (1995) 167–192.
[41] L. Ying, G. Biros, D. Zorin, A higher-order 3D boundary integral equation solver for elliptic PDEs in smooth domains, J. Comput. Phys. 219 (2006) 247–275.
[42] D. Saintillan, E. Darve, E. Shaqfeh, A smooth particle-mesh Ewald algorithm for Stokes suspension simulations: the sedimentation of fibers, Phys. Fluids 17 (2005) 033301.